Journal of Applied Physics

RESEARCH ARTICLE | APRIL 03 2023

Depth-dependent recovery of thermal conductivity after recrystallization of amorphous silicon

Kenny Huynh; Yekan Wang; Michael E. Liao; Thomas Pfeifer; John Tomko; Ethan Scott; Khalid Hattar; Patrick E. Hopkins; Mark S. Goorsky

Journal of Applied Physics 133, 135101 (2023)
https://doi.org/10.1063/5.0133548

CrossMark

Downloaded from http://pubs.aip.org/aip/jap/article-pdf/doi/10.1063/5.0133548/16824098/135101_1_5.0133548.pdf

Journal of Applied Physics | ARTICLE | scitation.org/journal/jap

Depth-dependent recovery of thermal conductivity after recrystallization of amorphous silicon

Cite as: J. Appl. Phys. **133**, 135101 (2023); doi: 10.1063/5.0133548
Submitted: 4 November 2022 · Accepted: 15 March 2023 ·
Published Online: 3 April 2023

View Online

Export Citation

CrossMark

Kenny Huynh,[1,a)] Yekan Wang,[1] Michael E. Liao,[1] Thomas Pfeifer,[2] John Tomko,[2] Ethan Scott,[2,3] Khalid Hattar,[3] Patrick E. Hopkins,[2] and Mark S. Goorsky[1]

AFFILIATIONS

[1]Department of Materials Science and Engineering, University of California, Los Angeles, Los Angeles, California 90095, USA
[2]Department of Mechanical and Aerospace Engineering, University of Virginia, Charlottesville, Virginia 22904, USA
[3]Sandia National Laboratories, Albuquerque, New Mexico 87185, USA

[a)]**Author to whom correspondence should be addressed:** huynhkenny@ucla.edu

ABSTRACT

The depth-dependent recovery of silicon thermal conductivity was achieved after the recrystallization of silicon that had been partially amorphized due to ion implantation. Transmission electron microscopy revealed nanoscale amorphous pockets throughout a structurally distorted band of crystalline material. The minimum thermal conductivity of as-implanted composite material was 2.46 W m^{-1} K^{-1} and was found to be uniform through the partially amorphized region. X-ray diffraction measurements reveal 60% strain recovery of the crystalline regions after annealing at 450 °C for 30 min and almost full strain recovery and complete recrystallization after annealing at 700 °C for 30 min. In addition to strain recovery, the amorphous band thickness reduced from 240 to 180 nm after the 450 °C step with nanoscale recrystallization within the amorphous band. A novel depth-dependent thermal conductivity measurement technique correlated thermal conductivity with the structural changes, where, upon annealing, the low thermal conductivity region decreases with the distorted layer thickness reduction and the transformed material shows bulk-like thermal conductivity. Full recovery of bulk-like thermal conductivity in silicon was achieved after annealing at 700 °C for 30 min. After the 700 °C anneal, extended defects remain at the implant projected range, but not elsewhere in the layer. Previous results showed that high point-defect density led to reduced thermal conductivity, but here, we show that point defects can either reform into the lattice or evolve into extended defects, such as dislocation loops, and these very localized, low-density defects do not have a significant deleterious impact on thermal conductivity in silicon.

Published under an exclusive license by AIP Publishing. https://doi.org/10.1063/5.0133548

INTRODUCTION

The effects of ion implantation on the microstructure of silicon[1,2] have been studied, but relatively few publications bridged the connection between thermal transport in ion implanted silicon and its microstructure.[3–5] Those studies hypothesized that strain (regardless of defect type) has detrimental effects on thermal conductivity, while Scott *et al.* have suggested that the reduction in thermal conductivity can be tracked by the damage profile (displacements per atom) based on ion species, dose, and implant energy.[6] Many earlier thermal studies of implanted silicon lacked detailed structural characterization to further support these hypotheses.

Ion implantation is known to cause distortions to the host lattice by introducing point defects, extended defects, and amorphization depending on the implant energy, temperature, dose, dose rate, and materials system. For heavier implanted species in silicon, it has been simulated[7,8] and experimentally observed[9–11] that small amorphous domains can form from single cascade events, creating a heterogeneous distribution of crystalline and amorphous domains near the implant projected range. This is unlike lighter implant species that have been shown to require multiple cascade events to eventually form a homogenous amorphous band of damage if the dose is sufficiently high.[12,13] From a thermal perspective, a mixture of amorphous domains and strained crystalline regions via ion

Downloaded from http://pubs.aip.org/aip/jap/article-pdf/doi/10.1063/5.0133548/16824098/135101_1_5.0133548.pdf

Published under an exclusive license by AIP Publishing

implantation will add additional thermal resistance. We show that strain from point defects and the inclusion of the nanoscale amorphous pockets have a detrimental effect on the thermal conductivity but can be fully recovered through annealing. For this study, silicon wafers implanted with Kr are investigated. Recovery of silicon thermal conductivity is achieved after recrystallization of partially amorphized silicon implanted with Kr ions, and x-ray and electron microscopy characterization is performed to complement the thermal results.

Detailed reports on the correlation between thermal conductivity and microstructure within radiation damaged ceramic materials (SiC, ThO_2, Si_3N_4, ZrN) exists in a combination of computational[14–18] and experimental work.[19–21] The difference between these studies and the current study is the use of MeV implantation energies, which induce amorphous regions tens of microns into the substrate. In doing so, thermal conductivity measurements are able to probe the top few microns and isolate the damaged layer that is assumed to have homogeneous properties. Then, commonly used three-layer fitting methods probe depth-dependent thermal conductivity by utilizing the assumptions that each layer (damaged, amorphous, pristine) in an irradiated sample has homogeneous thermal properties.[22–25]

The implant conditions used in this study generate an amorphous region in silicon with a non-uniform distribution of defects and a shallow implant range (∼300 nm). This implanted structure has necessitated a finer assessment of thermal conductivity with depth in order to resolve the non-uniform distribution of defects. A mixture of nanocrystalline and amorphous regions exist in the damaged layer, which would not suggest homogeneous thermal conductivity within this region. In this study, we utilize quantitative structural analysis to better understand how the thermal conductivity of silicon is modified with both strained and amorphous regions and how the thermal conductivity of these regions changes with subsequent annealing. In particular, a novel, depth-dependent thermal conductivity technique[26] is used to better connect the distribution of defects with variations in thermal conductivity with finer depth resolution.

EXPERIMENTAL METHODS

(001) silicon was implanted with 500 keV Kr ions at a dose of 1×10^{14} ions cm^{-2}. Bombardment was performed using a 3 MeV Pelletron implanter and performed at a few degrees from the surface normal. Sample 1 represents the as-implanted conditions. Sample 2 was annealed at 450 °C for 30 min in ambient air. Sample 3 was annealed at 700 °C for 30 min in ambient air. An FEI Nova 600 Nanolab Dual Beam SEM/FIB was used to prepare cross-sectional TEM samples roughly 100 nm thick using a Ga source and transferred to a TEM grid using a standard lift out procedure. High resolution transmission electron microscopy (HRTEM) images were taken using an FEI Titan and a double tilt stage at 300 kV to study the crystallinity and defect structure evolution at each annealing stage. Triple axis x-ray measurements used a Bruker D1 diffractometer with an incident beam mirror producing a parallel beam and a Si (220) channel cut collimator (Cu kα_1 radiation). The scattered beam optics include a Si (220) channel cut crystal. Bruker RADS software[27] was used to fit and model experimental measurements to quantitatively analyze strain due to implantation. The Stopping Ranges of Ions in Matter (SRIM) software[28] was used to simulate and predict ion distributions and vacancy concentrations after implantation.

Thermal measurements were performed via time domain thermoreflectance (TDTR). TDTR is an optical pump-probe technique wherein a pulsed laser is used to heat the sample surface (pump) and subsequently measure the changes in reflectivity (probe), which is indicative of the temperature rise. By changing the time delay between the arrival of pump and probe pulses, the temperature decay can be found, and an analytical thermal model is then used to fit for unknown thermal properties. This technique also requires the deposition of a thin metal film, which limits the optical penetration (heating) of the pump to the surface and provides an optically reflective surface for the probe. Our TDTR system is comprised of an 800 nm wavelength Ti:sapphire laser pulsed at 80 MHz. The pump beam is modulated at frequencies between 2 and 8.4 MHz, which allows lock-in detection of the probe and sensitivity to thermal properties at varying depths based on frequency. We use an 80 nm aluminum transducer, deposited via e-beam evaporation following ion irradiation. The surface of the silicon is washed prior to aluminum deposition, using methanol, acetone, isopropyl alcohol, and O_2 plasma cleaned for 30 min, which ensures that a strong bond between the aluminum and substrate is obtained.

In the case of ion bombarded solids, a slight modification to the thermal analysis should be considered in order to account for the depth-varying thermal conductivity due to irradiation. This analysis is discussed in depth in our prior work,[26] but in summary, the thermal model is discretized into a series of layers with an infinite thermal boundary conductance between them (zero thermal boundary resistance). Given that the ion irradiation creates a Gaussian-like distribution of damage, we then set the thermal resistivity for each layer according to a Gaussian function. The TDTR temperature decay data are then used to fit for the Gaussian center,

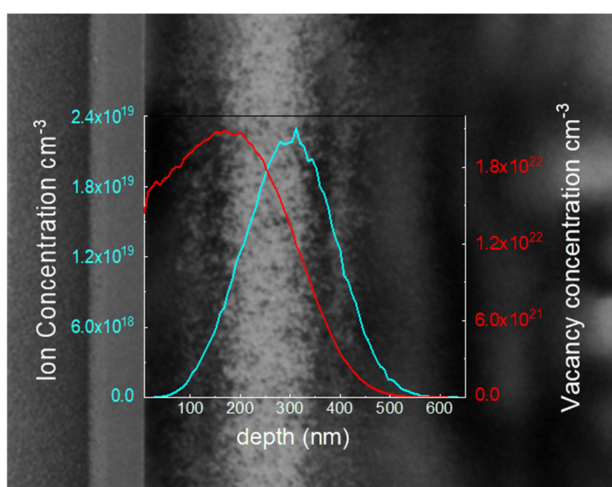

FIG. 1. SRIM profiles simulating the ion and vacancy distributions, which are overlayed onto the as-implanted bright field TEM (BFTEM) image.

Downloaded from http://pubs.aip.org/aip/jap/article-pdf/doi/10.1063/5.0133548/16824098/135101_1_5.0133548.pdf

Published under an exclusive license by AIP Publishing

FIG. 2. Filtered HRTEM image of the as-implanted sample near the peak of damage due to implantation. Nanoscale sized domains (5–10 nm in diameter) are distributed throughout the distorted band parallel to the surface of the sample. FFTs of these regions provide evidence of crystalline and amorphous structures.

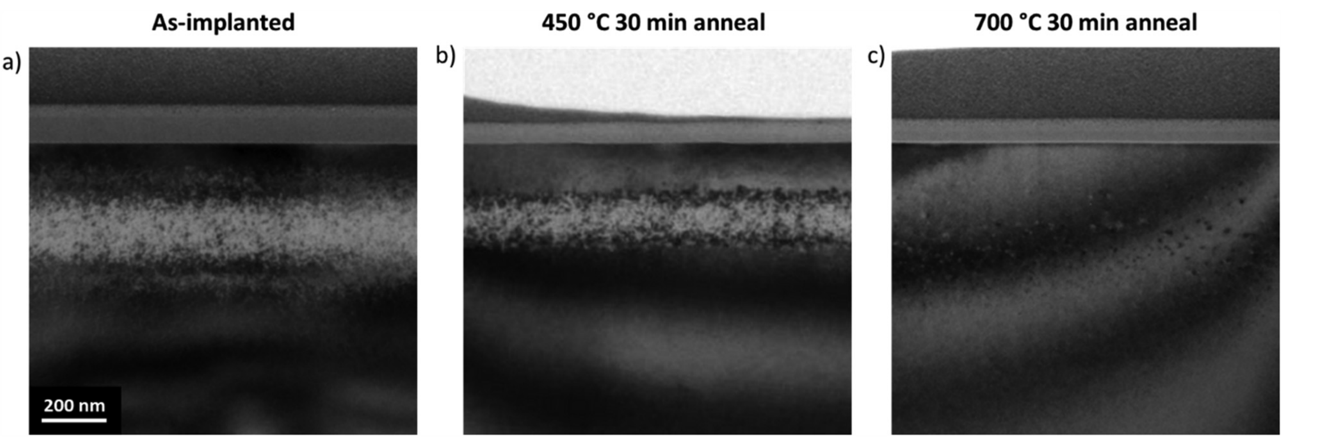

FIG. 3. BFTEM image for the (a) as-implanted, (b) 450 °C 30 min, and (c) 700 °C 30 min annealed samples. Comparison of (a) and (b) reveal the beginning of recrystallization as the thickness of the distorted region shrinks. After complete recrystallization seen in (c), extended defects are left distributed near the projected range of implant.

Downloaded from http://pubs.aip.org/aip/jap/article-pdf/doi/10.1063/5.0133548/16824098/135101_1_5.0133548.pdf

Published under an exclusive license by AIP Publishing

width, and minimum conductivity, plus the thermal boundary conductance between the transducer and silicon.

RESULTS

SRIM simulations predict a peak ion concentration of 4.5×10^{18} cm^{-3} at ∼310 nm from the surface and a peak vacancy concentration due to displacements at a depth of 180 nm. This projected range compares well to TEM imaging in the as-implanted sample as seen in Fig. 1. TEM of the as-implanted silicon sample reveals a structurally distorted band that begins roughly 150 nm below the surface and is 240 nm wide. Close inspection throughout the distorted region shows pockets of amorphous silicon domains that range from 5 to 10 nm in diameter embedded in the crystalline silicon lattice. This observation is supported by localized fast Fourier transforms that reveal diffuse rings in the amorphous regions and well defined diffraction patterns in the crystalline regions shown in Fig. 2. Amorphous domains in the as-implanted sample make up roughly 53% of the area in the distorted band as estimated from bright field TEM images, where amorphous regions do not strongly diffract the direct beam and, therefore, appear brighter than their crystalline counterparts.

After annealing at 450 °C for 30 min, partial recrystallization is observed as the thickness of the distorted band shrinks roughly 60 nm (to ∼180 nm thickness) from the bottom amorphous–crystalline interface. Recrystallization via solid phase epitaxy occurs at the crystalline boundary beyond the projected range rather than from both sides of the distorted band. This is comparing the distorted layer thickness in Figs. 3(a) and 3(b). Additionally, recrystallization also occurs within the distorted band itself and originates at the crystalline domains as solid phase epitaxy as well. This is evidenced by larger crystalline domains with diameters of 4.8 ± 1.5 nm (as implanted) and 12 ± 5.4 nm (450 °C) and a reduction in the fraction of a total amorphous area from 53% to 34% as shown in Fig. 4. Complete recrystallization occurred after annealing at 700 °C for 30 min as shown by selective area diffraction measurements throughout the sample that revealed sharp diffraction spots. However, extended defects were present and concentrated near the projected range with a density of 6.25×10^{15} cm^{-3}.

Triple axis ω:2θ x-ray scans were taken to assess lattice strain after implantation and after each annealing step. Figure 5 compares the symmetric (004) Si ω:2θ line scans of the as-implanted, 450 °C 30 min, and 700 °C 30 min samples. In the as-implanted sample, well defined strain fringes toward lower angular values indicate out of plane tensile strain. After each progressive annealing condition, the shoulder recedes toward the main peak, indicating strain reduction. For in-depth strain analysis, x-ray dynamical simulations using Bruker RADS software provide quantitative information about the strain-inducing implant species and the elastic deformation of the lattice after implantation. The simulation process is very similar to our earlier implantation studies.[29–36] However, in order to account for the presence of amorphous domains in the as-implanted sample and the 450 °C annealed sample, we created a quasi-Si structure by modifying the scattering factor for the amorphous regions. Because TEM showed complete recrystallization at 700 °C, a regular Si model is used in the fitting for that case. A strong fit between the simulated and experimental ω:2θ scans was observed for all three samples, suggesting that the modified structures successfully mimic the lattice disorder in the real samples. Figure 6 shows the comparison between the simulated fits in each case. 60% of the strain is recovered after annealing at 450 °C for

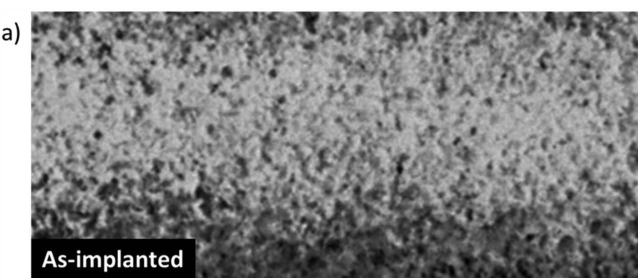

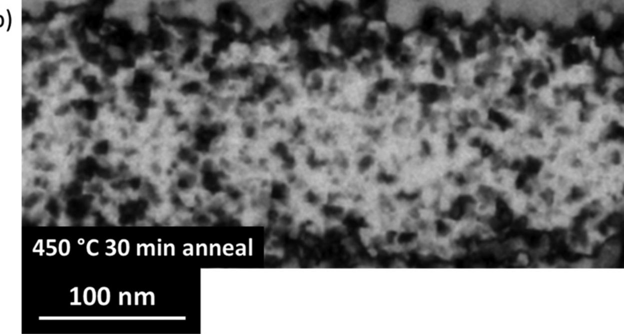

FIG. 4. Higher magnification BFTEM of the (a) as-implanted and (b) 450 °C 30 min annealed sample. Comparison of the two shows a decrease in the total fraction of amorphous regions from 53% to 34% after the first annealing step.

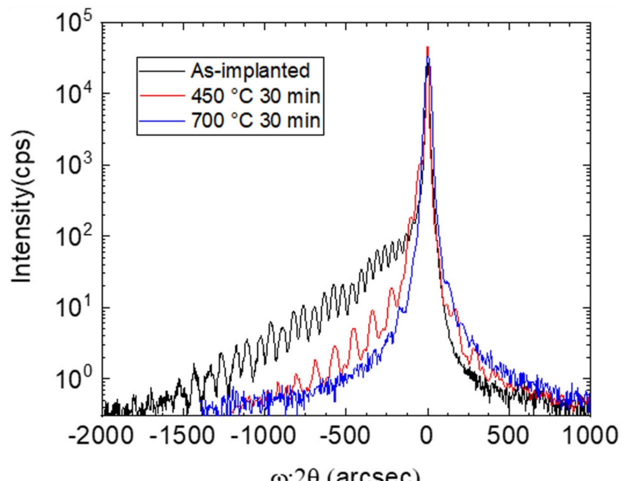

FIG. 5. Triple axis diffraction ω:2θ (004) Si line scans show a reduction in strain fringes after each progressive annealing step.

Downloaded from http://pubs.aip.org/aip/jap/article-pdf/doi/10.1063/5.0133548/16824098/135101_1_5.0133548.pdf

Published under an exclusive license by AIP Publishing

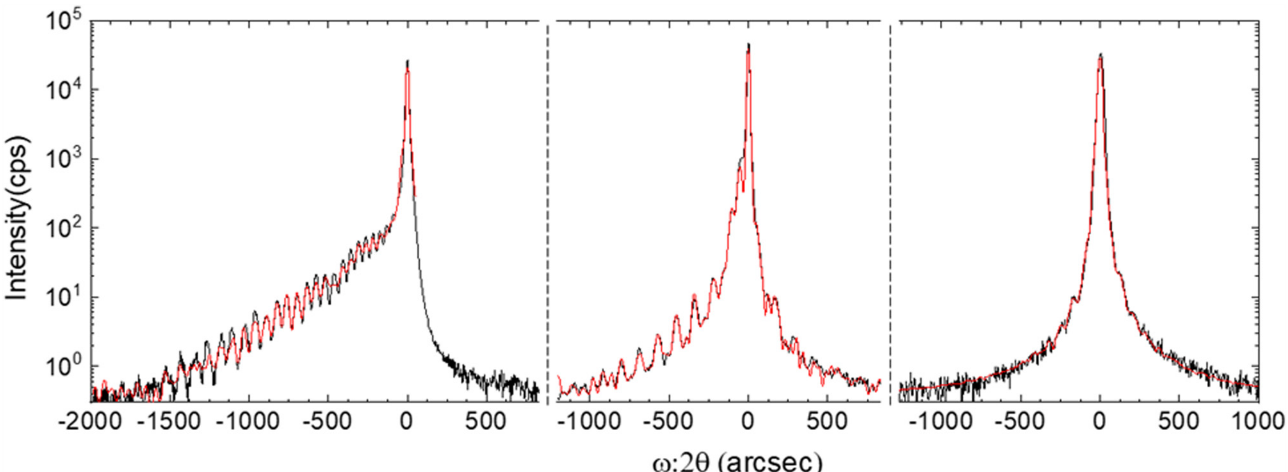

FIG. 6. RADS fitting overlayed on experimental ω:2θ scans. To account for the presence of amorphous domains in the as-implanted sample and the 450 °C annealed sample, a quasi-Si structure was made by replacing part of the Si atoms on the lattice with H atoms. Since TEM showed complete recrystallization at 700 °C, a regular Si model is used in the fitting. Peak strain of the as-implanted (left), 450 °C (middle), and 700 °C (right) samples is 4300, 1700, and 110 ppm, respectively.

30 min, and over 97% of the point-defect induced strain is recovered after annealing at 700 °C for 30 min.

In contrast to thermal metrology techniques that assume uniform material properties,[37–40] modifications have been made to the time domain thermal reflectance analysis, which has allowed the measurement of thermal conductivity as a function of depth with a non-uniform defect distribution.[26] This is useful for understanding the effects of ion implantation where regions of amorphous and strained crystalline domains are observed as a function of depth in silicon. Spatially varying time domain thermoreflectance measurements as a function of depth shown in Fig. 7 measure a minimum thermal conductivity of $2.5 \pm 0.7\ \mathrm{W\,m^{-1}\,K^{-1}}$ at 250 ± 20 nm in the as implanted sample, $3.2 \pm 0.8\ \mathrm{W\,m^{-1}\,K^{-1}}$ at 270 ± 20 nm in the sample annealed at 450 °C, and fully recovered thermal conductivity within error of bulk silicon ($130\ \mathrm{W\,m^{-1}\,K^{-1}}$) in the fully recrystallized sample annealed at 700 °C. Rigorous uncertainty analysis and detailed information on the thermal conductivity measurements can be found in Pfeifer *et al.*[26] In addition, the depth-dependent thermal conductivity mimics the structural changes seen in TEM, where the low thermal conductivity region shrinks alongside with the decrease in the distorted region layer thickness after the annealing at 450 °C.

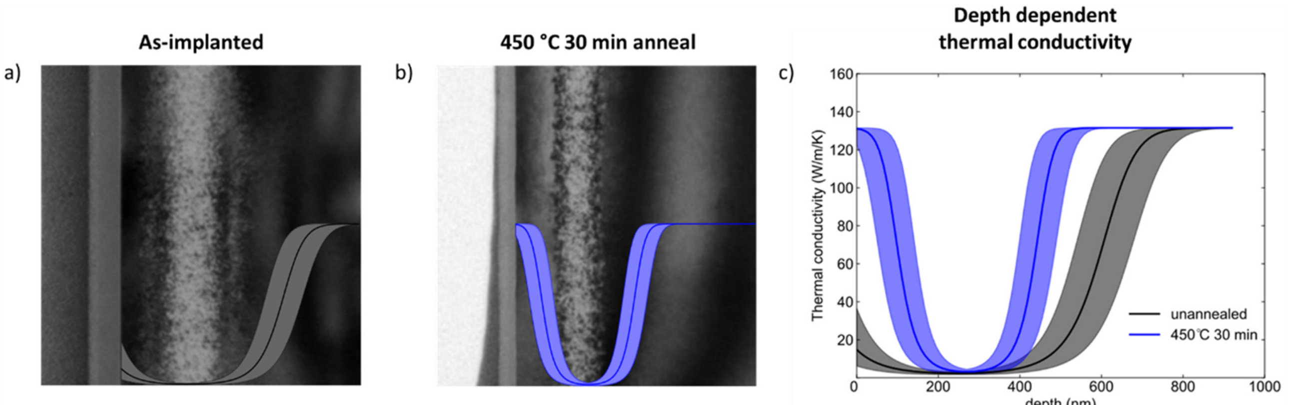

FIG. 7. Depth-dependent thermal conductivity measurements overlaid on the BFTEM images reveal how the thermal conductivity is recovered as the distorted band shrinks and as strain is relieved. The solid line represents the nominal best fit, and the shaded region represents the uncertainty corresponding to fitted functions yielding 2.5% residual.

Downloaded from http://pubs.aip.org/aip/jap/article-pdf/doi/10.1063/5.0133548/16824098/135101_1_5.0133548.pdf

Published under an exclusive license by AIP Publishing

DISCUSSION

The critical dose of amorphization of silicon can be estimated as a function of the ion beam energy, straggle (from SRIM), atomic density, and displacement energy of Si.[41] For our system, the critical dose is calculated to be $\sim 6.5 \times 10^{13}$ ions cm^{-2}, slightly below the 10^{14} ions cm^{-2} dose used in this experiment. For heavy ion implants, amorphous pockets have been observed to form from single cascade events, even below the critical dose.[7,9–13] The experimental parameters set here approach a regime where the amorphous pockets become so dense that they nearly form a homogenous amorphous layer. Instead, nanoscale domains of amorphous and crystalline material are distributed throughout the distorted band in the as-implanted sample. This phenomenon has been observed before when the implanted dose approached the estimated critical dose of amorphization.[42]

From a thermal perspective, previous studies showed that the strain caused by point defects was found to be the dominating contributor to the reduction in thermal conductivity in ion implanted semiconductors.[4,6] Our findings agree with these results, and we show that after annealing at 450 °C for 30 min, the strain has sufficiently recovered near the edges of the distorted region and improvements in the thermal conductivity are observed. However, even after a 60% reduction in the peak strain, the minimum thermal conductivity measured remains the same as the as-implanted sample. To our knowledge, no studies have recorded the evolution of strain and thermal conductivity with annealing and only the initial and final stages of pre-anneal and full recrystallization.[6] However, in a similar study, Scott *et al.* implanted Si with $^{28}Si^{+}$ at various incremental doses, which mimic gradually increasing strain states in silicon.[4] In their study, they observed monotonically decreasing thermal conductivity from 110 to 40 $W\,m^{-1}\,K^{-1}$ with increasing dose from 6.23×10^{13} to 6.24×10^{16} ions cm^{-2}, respectively. As seen in our 450 °C 30 min anneal case, there remains sufficient distortion in the crystal to maintain the low value of thermal conductivity in the distorted region but recovery of the thermal conductivity in the epitaxially regrown regions. Boundary scattering between amorphous and crystalline regions was hypothesized to be dominant in explaining the low thermal conductivity in the unannealed case,[26] and this effect may also explain the similar maximum reduction in thermal conductivity in the 450 °C anneal case. After complete recrystallization when annealing at 700 °C for 30 min, the measured thermal conductivity is fully recovered and matches un-irradiated silicon within uncertainty. Dislocation loops do form near the projected range during the recrystallization process as a result of the agglomeration of point defects that reduces the strain, a process that has been systematically studied previously.[2] This matches well with our x-ray measurements and simulations that show complete strain reduction in the layer and over 97% reduction in the region that had been most highly strained. The presence of the dislocation loops in these materials apparently does not have a measurable deleterious impact on the thermal conductivity as the conductivity is uniform as a function of depth in that case.

CONCLUSION

We have demonstrated complete recovery of thermal conductivity in partially amorphized Si implanted with 10^{14} Kr ions cm^{-2} at 500 keV. Quantitative structural analysis is performed for an as-implanted, 450 °C 30 min anneal, and 700 °C 30 min anneal, which shows strain reduction at each progressive annealing step. Comparison of the high resolution TEM of the as-implanted and 450 °C sample reveals progress toward recrystallization, where the area fraction of the amorphous domains is reduced from 53% to 34% within the distorted band. In addition, recrystallization occurs at the bottom amorphous–crystalline interface where we observe shrinkage of the distorted band. Depth-dependent thermal conductivity measurements mimic these structural changes where the low thermal conductivity region shrinks as strain is relieved. Finally, when complete recrystallization occurs, in addition to point defects returning to lattice sites, extended defects are formed during the recovery process to reduce the overall strain in the crystal, as evidenced by our x-ray scattering measurements. After the 700 °C anneal, the thermal conductivity is fully recovered and is uniform throughout the depth of the layer. The 450 °C annealing condition prior to full recrystallization of the distorted region reveals that the thermal conductivity progressively recovers after the removal of the amorphous pockets and after reduction in the point-defect induced strain. While the peak strain is reduced by over 60%, the minimum thermal conductivity within the center of the distorted region remains unchanged. This suggests that the nanoscale amorphous regions dominate the reduction in thermal conductivity prior to complete recovery and demonstrate the potential for the recently developed depth-dependent thermal measurements.

ACKNOWLEDGMENTS

This work was supported by the Office of Naval Research MURI (Grant No. N00014-18-1-2429).

This material is based upon work supported by the National Science Foundation Graduate Research Fellowship Program under Grant No. DGE-2034835. Any opinions, findings, and conclusions or recommendations expressed in this material are those of the author(s) and do not necessarily reflect the views of the National Science Foundation.

This work was performed, in part, at the Center for Integrated Nanotechnologies, an Office of Science User Facility operated for the U.S. Department of Energy (DOE) Office of Science. Sandia National Laboratories is a multimission laboratory managed and operated by the National Technology & Engineering Solutions of Sandia, LLC, a wholly owned subsidiary of Honeywell International, Inc., for the U.S. DOE's National Nuclear Security Administration under Contract No. DE-NA-0003525. The views expressed in the article do not necessarily represent the views of the U.S. DOE or the United States Government.

AUTHOR DECLARATIONS

Conflict of Interest

The authors have no conflicts to disclose.

Author Contributions

Kenny Huynh: Conceptualization (lead); Data curation (lead); Formal analysis (lead); Investigation (lead); Methodology (lead); Project administration (lead); Visualization (lead); Writing –

Downloaded from http://pubs.aip.org/aip/jap/article-pdf/doi/10.1063/5.0133548/16824098/135101_1_5.0133548.pdf

Published under an exclusive license by AIP Publishing

original draft (lead); Writing – review & editing (lead). **Yekan Wang:** Conceptualization (supporting); Data curation (supporting); Formal analysis (supporting); Investigation (supporting); Methodology (supporting); Visualization (supporting); Writing – review & editing (supporting). **Michael E. Liao:** Conceptualization (supporting); Data curation (supporting); Formal analysis (supporting); Investigation (supporting); Methodology (supporting); Writing – review & editing (supporting). **Thomas Pfeifer:** Data curation (supporting); Formal analysis (supporting); Investigation (supporting); Methodology (supporting); Visualization (supporting); Writing – review & editing (supporting). **John Tomko:** Data curation (supporting); Formal analysis (supporting); Methodology (supporting); Writing – review & editing (supporting). **Ethan Scott:** Data curation (supporting); Formal analysis (supporting); Methodology (supporting); Resources (supporting); Writing – review & editing (supporting). **Khalid Hattar:** Investigation (supporting); Resources (supporting); Supervision (supporting); Writing – review & editing (supporting). **Patrick E. Hopkins:** Data curation (supporting); Formal analysis (supporting); Funding acquisition (equal); Methodology (supporting); Project administration (supporting); Supervision (supporting); Writing – review & editing (supporting). **Mark S. Goorsky:** Conceptualization (supporting); Data curation (supporting); Formal analysis (supporting); Funding acquisition (equal); Methodology (supporting); Project administration (supporting); Resources (supporting); Supervision (lead); Visualization (supporting); Writing – original draft (supporting); Writing – review & editing (equal).

DATA AVAILABILITY

The data that support the findings of this study are available from the corresponding author upon reasonable request.

REFERENCES

[1]J. L. Benton, S. Libertino, P. Kringho/j, D. J. Eaglesham, J. M. Poate, and S. Coffa, J. Appl. Phys. **82**(1), 120–125 (1997).
[2]K. S. Jones, S. Prussin, and E. R. Weber, Appl. Phys. A Solids Surf. **45**(1), 1–34 (1988).
[3]M. Khafizov, C. Yablinsky, T. R. Allen, and D. H. Hurley, Nucl. Instrum. Methods Phys. Res. Sect., B **325**, 11–14 (2014).
[4]E. A. Scott, K. Hattar, C. M. Rost, J. T. Gaskins, M. Fazli, C. Ganski, C. Li, T. Bai, Y. Wang, K. Esfarjani, M. Goorsky, and P. E. Hopkins, Phys. Rev. Mater. **2**(9), 095001 (2018).
[5]E. A. Scott, K. Hattar, J. L. Braun, C. M. Rost, J. T. Gaskins, T. Bai, Y. Wang, C. Ganski, M. S. Goorsky, and P. E. Hopkins, Carbon **157**, 97–105 (2020).
[6]E. A. Scott, K. Hattar, E. J. Lang, K. Aryana, J. T. Gaskins, and P. E. Hopkins, Phys. Rev. B **104**(13), 134306 (2021).
[7]M.-J. Caturla, T. D. de La Rubia, L. A. Marques, and G. H. Gilmer, Phys. Rev. B **54**(23), 16683 (1996).
[8]H. Hensel and H. M. Urbassek, Phys. Rev. B **57**(8), 4756–4763 (1998).
[9]M. O. Ruault, J. Chaumont, J. M. Penisson, and A. Bourret, Philos. Mag. A **50**(5), 667–675 (1984).
[10]L. M. Howe and M. H. Rainville, Nucl. Instrum. Methods **182–183**, 143–151 (1981).
[11]L. M. Howe and M. H. Rainville, Nucl. Instrum. Methods Phys. Res. Sect., B **19–20**, 61–66 (1987).
[12]L. Pelaz, L. A. Marqués, and J. Barbolla, J. Appl. Phys. **96**(11), 5947–5976 (2004).
[13]F. Priolo, A. Battaglia, R. Nicotra, and E. Rimini, Appl. Phys. Lett. **57**(8), 768–770 (1990).
[14]J. Li, L. Porter, and S. Yip, J. Nucl. Mater. **255**(2), 139–152 (1998).
[15]J.-P. Crocombette and L. Proville, Appl. Phys. Lett. **98**(19), 191905 (2011).
[16]J. Park, E. B. Farfán, K. Mitchell, A. Resnick, C. Enriquez, and T. Yee, J. Nucl. Mater. **504**, 198–205 (2018).
[17]D. H. Hurley, A. El-Azab, M. S. Bryan, M. W. D. Cooper, C. A. Dennett, K. Gofryk, L. He, M. Khafizov, G. H. Lander, M. E. Manley, J. M. Mann, C. A. Marianetti, K. Rickert, F. A. Selim, M. R. Tonks, and J. P. Wharry, Chem. Rev. **122**(3), 3711–3762 (2022).
[18]R. A. Rymzhanov, A. Akzhunussov, A. E. Volkov, A. D. Ibrayeva, and V. A. Skuratov, Nucl. Mater. Energy **33**, 101267 (2022).
[19]C. A. Dennett, W. R. Deskins, M. Khafizov, Z. Hua, A. Khanolkar, K. Bawane, L. Fu, J. M. Mann, C. A. Marianetti, L. He, and D. H. Hurley, Acta Mater. **213**, 116934 (2021).
[20]A. Reza, G. He, C. A. Dennett, H. Yu, K. Mizohata, and F. Hofmann, Acta Mater. **232**, 117926 (2022).
[21]A. Prosvetov, G. Hamaoui, N. Horny, M. Chirtoc, F. Yang, C. Trautmann, and M. Tomut, Acta Mater. **184**, 187–198 (2020).
[22]J. Cabrero, F. Audubert, R. Pailler, A. Kusiak, J. L. Battaglia, and P. Weisbecker, J. Nucl. Mater. **396**(2), 202–207 (2010).
[23]A. Abdullaev, V. S. Chauhan, B. Muminov, J. O'Connell, V. A. Skuratov, M. Khafizov, and Z. N. Utegulov, J. Appl. Phys. **127**(3), 035108 (2020).
[24]Z. Hua, A. Fleming, and H. Ban, Int. J. Heat Mass Transfer **131**, 206–216 (2019).
[25]M. F. Riyad, V. Chauhan, and M. Khafizov, J. Nucl. Mater. **509**, 134–144 (2018).
[26]T. W. Pfeifer, J. A. Tomko, E. Hoglund, E. A. Scott, K. Hattar, K. Huynh, M. Liao, M. Goorsky, and P. E. Hopkins, J. Appl. Phys. **132**(7), 075112 (2022).
[27]RADS SOFTWARE, Bruker Semiconductor, info.semi@bruker.com.
[28]J. F. Ziegler and J. P. Biersack, *The Stopping and Range of Ions in Matter* (Springer US, Boston, MA, 1985), pp. 93–129.
[29]Y. Wang, T. Bai, C. Li, M. J. Tadjer, T. J. Anderson, J. K. Hite, M. A. Mastro, C. R. Eddy, K. D. Hobart, B. N. Feigelson, and M. S. Goorsky, ECS J. Solid State Sci. Technol. **8**, P70–P76 (2019).
[30]Y. Wang, K. Huynh, M. E. Liao, H.-M. Yu, T. Bai, J. Tweedie, M. H. Breckenridge, R. Collazo, Z. Sitar, M. Bockowski, Y. Liu, and M. S. Goorsky, Phys. Status Solidi B **257**, 1900705 (2020).
[31]C. Miclaus and M. S. Goorsky, J. Phys. D: Appl. Phys. **36**(10A), A177–A180 (2003).
[32]S. T. Horng and M. S. Goorsky, Appl. Phys. Lett. **68**(11), 1537–1539 (1996).
[33]S. T. Horng, M. S. Goorsky, J. H. Madok, and N. M. Haegel, J. Appl. Phys. **76**(4), 2066–2069 (1994).
[34]I. P. Ferain, K. Y. Byun, C. A. Colinge, S. Brightup, and M. S. Goorsky, J. Appl. Phys. **107**(5), 054315 (2010).
[35]M. E. Liao, Y. Wang, T. Bai, and M. S. Goorsky, ECS J. Solid State Sci. Technol. **8**(11), P673–P676 (2019).
[36]S. Hayashi, R. Sandhu, and M. S. Goorsky, J. Electrochem. Soc. **154**(4), H293 (2007).
[37]D. G. Cahill, Rev. Sci. Instrum. **61**(2), 802–808 (1990).
[38]D. G. Cahill, Rev. Sci. Instrum. **75**(12), 5119–5122 (2004).
[39]A. J. Schmidt, R. Cheaito, and M. Chiesa, Rev. Sci. Instrum. **80**(9), 094901 (2009).
[40]J. L. Braun, D. H. Olson, J. T. Gaskins, and P. E. Hopkins, Rev. Sci. Instrum. **90**(2), 024905 (2019).
[41]S. K. Ghandhi, *VLSI Fabrication Principles: Silicon and Gallium Arsenide* (John Wiley & Sons, 2008).
[42]J. Narayan and O. W. Holland, J. Electrochem. Soc. **131**(11), 2651–2662 (1984).

Downloaded from http://pubs.aip.org/aip/jap/article-pdf/doi/10.1063/5.0133548/16824098/135101_1_5.0133548.pdf

Published under an exclusive license by AIP Publishing